

The cool supergiant population of the massive young star cluster RSGC1

Ben Davies¹, Don F. Figer¹, Casey J. Law², Rolf-Peter Kudritzki³, Francisco Najarro⁴,
Artemio Herrero⁵ and John W. MacKenty⁶

¹*Chester F. Carlson Center for Imaging Science, Rochester Institute of Technology, 54
Lomb Memorial Drive, Rochester NY, 14623, USA*

²*Astronomical Institute "Anton Pannekoek", University of Amsterdam, Kruislaan 403,
1098 SJ, Amsterdam, The Netherlands*

³*Institute for Astronomy, University of Hawaii, 2680 Woodlawn Drive, Honolulu, HI,
96822, USA*

⁴*Instituto de Estructura de la Materia, Consejo Superior de Investigaciones Cientificas,
Calle Serrano 121, 28006 Madrid, Spain.*

⁵*Instituto de Astrofísica de Canarias, Via Láctea S/N, E-38200 La Laguna, Tenerife, Spain*

⁶*Space Telescope Science Institute, 3700 San Martin Drive, Baltimore, MD 21218*

ABSTRACT

We present new high-resolution near-IR spectroscopy and OH maser observations to investigate the population of cool luminous stars of the young massive Galactic cluster RSGC1. Using the $2.293\mu\text{m}$ CO-bandhead feature, we make high-precision radial velocity measurements of 16 of the 17 candidate Red Supergiants (RSGs) identified by Figer et al. We show that F16 and F17 are foreground stars, while we confirm that the rest are indeed physically-associated RSGs. We determine that Star F15, also associated with the cluster, is a Yellow Hypergiant based on its luminosity and spectroscopic similarity to ρ Cas. Using the cluster's radial velocity, we have derived the kinematic distance to the cluster and revisited the stars' temperatures and luminosities. We find a larger spread of luminosities than in the discovery paper, consistent with a cluster age 30% older than previously thought ($12\pm 2\text{Myr}$), and a total initial mass of $(3\pm 1)\times 10^4 M_{\odot}$. The spatial coincidence of the OH maser with F13, combined with similar radial

velocities, is compelling evidence that the two are related. Combining our results with recent SiO and H₂O maser observations, we find that those stars with maser emission are the most luminous in the cluster. From this we suggest that the maser-active phase is associated with the end of the RSG stage, when the luminosity-mass ratios are at their highest.

Subject headings: open clusters & associations, supergiants, stars:evolution, stars:late-type, masers

1. Introduction

The Red Supergiants (RSGs) represent a key evolutionary phase in the life-cycle of stars with initial masses of $\sim 8\text{--}30M_{\odot}$ (e.g. Meynet & Maeder 2000). Though comparatively brief, the mass-loss rate in this stage can be many orders of magnitude greater than on the main-sequence (e.g. Repolust et al. 2004; van Loon et al. 2005), and the mass lost in the RSG phase can determine the terminal mass of the star, the appearance of the supernova (SN) explosion, and nature of the stellar remnant (e.g. Heger et al. 2003).

The study of RSGs is hampered by low-number statistics – until recently only ~ 200 were known in the Galaxy, and around 40 in the Large Magellanic Cloud (LMC). Further, the majority of these stars are isolated, and hence have a variety of ages, initial masses and metallicities. Ideally, we would like to study large numbers of RSGs *coeval clusters*, where we can be confident that the variables of metallicity and initial stellar mass are fixed.

Two recent discoveries now present us with the opportunity to study statistically-significant numbers of RSGs in such clusters. In Figer et al. (2006, hereafter FMR06) the discovery of an apparent cluster of 14 RSGs was presented; while Davies et al. (2007, hereafter DFK07) report on the remarkable stellar population of a second cluster in the same region, which it was shown contains 26 RSGs. In order to use these two clusters as testbeds with which to study the pre-SN evolution of massive stars, we must first quantitatively study the properties of the stars within each.

In the case of the second cluster, hereafter RSGC2 (also known as Stephenson 2), DFK07 used high-resolution spectroscopy to obtain accurate radial velocities of many stars in the region of the cluster, and were able to separate proper cluster-members from background/foreground stars. Further, from the radial velocities they made a quantitative discussion of the kinematic distance to the cluster, thus enabling them to determine the stars' luminosities, temperatures, ages and initial masses.

The details of the stellar properties of the first cluster, hereafter RSGC1, are less well constrained. In the discovery paper FMR06 showed with low-resolution spectra that the stars were all late-type; but with no radial velocity information, they relied on the stars’ similar near-IR colours to argue that the stars were all at the same distance. They determined this distance by associating a nearby OH maser, detected by Blommaert et al. (1994), with the RSGs. However this maser was *singly-peaked* – such masers are formed in the winds of RSGs and hence are typically *doubly-peaked*, with separation twice the outflow speed. If the second peak was missed in the original observations, this would lead to an incorrect radial velocity for the cluster, and hence kinematic distance. Consequently, the cluster membership, as well as the properties of the luminous cool stars of RSGC1 are poorly-constrained when compared to RSGC2.

Here, we study the cool supergiants of RSGC1 with data of similar quality to that presented in DFK07 for RSGC2. We present high resolution spectroscopy of the CO bandhead feature of 16 of the 17 *K*-bright stars in the field identified in FMR06, allowing us to determine accurate radial velocities of the stars, and establish the cluster membership. We also present new observations of the OH maser source OH25.25-0.16, showing that it is indeed doubly-peaked, and that the central radial velocity of the profile is consistent with the average stellar radial velocity. We use this value, in conjunction with contemporary Galactic rotation curve parameters, to reappraise the distance to the cluster, the stars’ temperatures and luminosities, and the age and initial mass of the cluster.

We begin in Sect. 2 with a description of the observations and data reduction steps, and we describe the results and analysis of the data in Sect. 3. In Sect. 4 we derive the cluster’s age and mass, and compare with similar analyses of RSGC2. Finally, we use the stellar population of RSGC1 to investigate the maser-active phase of RSGs.

2. Observations & data reduction

2.1. Radio observations & data reduction

OH maser observations at 18 cm were carried out with the VLA¹ on 25 May, 2006 in the AB configuration. The 256-channel spectrum had a bandwidth of 1.56 MHz giving a velocity resolution of 1.1 km s⁻¹ and was centered at $v_{\text{LSR}} = 100$ km s⁻¹. The observation consisted of a single pointing with J2000 coordinates of (18h37m52s,-06°53’40’’) and had a

¹The Very Large Array (VLA) is operated by the National Radio Astronomy Observatory under cooperative agreement with the National Science Foundation.

Table 1:: Data for the stars observed. Designations are from FMR06, coordinates and apparent magnitudes are from 2MASS.

ID	α	δ	m_J	m_H	m_{K_S}
J2000					
F01	18 37 56.29	-6 52 32.2	9.748	6.587	4.962
F02	18 37 55.28	-6 52 48.4	9.904	6.695	5.029
F03	18 37 59.72	-6 53 49.4	9.954	6.921	5.333
F04	18 37 50.90	-6 53 38.2	9.658	6.803	5.342
F05	18 37 55.50	-6 52 12.2	10.547	7.178	5.535
F06	18 37 57.45	-6 53 25.3	9.866	7.038	5.613
F07	18 37 54.31	-6 52 34.7	9.941	7.065	5.631
F08	18 37 55.19	-6 52 10.7	10.772	7.330	5.654
F09	18 37 57.77	-6 52 22.2	10.262	7.240	5.670
F10	18 37 59.53	-6 53 31.9	10.179	7.218	5.709
F11	18 37 51.72	-6 51 49.9	10.467	7.325	5.722
F12	18 38 3.30	-6 52 45.1	10.143	7.238	5.864
F13	18 37 58.90	-6 52 32.1	10.907	7.716	5.957
F14	18 37 47.63	-6 53 2.3	10.495	7.576	6.167
F15	18 37 57.78	-6 52 32.0	10.651	8.070	6.682
F16	18 38 1.30	-6 52 52.0	13.617	9.608	7.558
F17	18 37 48.77	-6 53 7.7	12.763	10.188	9.003

field of view of about $27'$. The beam size is $3.5'' \times 1.8''$. The total integration time was 340 minutes, giving an rms error of about 4 mJy beam^{-1} per 4 kHz channel.

The data were calibrated using the AIPS package. The flux and bandpass calibrator was 1331+305, while 1822-096 was used as a phase calibrator. The phase calibrator was mildly resolved in this observation, so baselines with uv distances greater than $50 k\lambda$ were removed when solving for a phase solution. Minimal flagging was required to remove interference. The astrometric accuracy of our positions is dominated by the uncertainty in the position of our phase calibration source, which is $0.3''$. The compact source GPSR5 25.266-0.161 has a J2000 position of (18h37m57.9934s, $-06^\circ 53' 30.973''$), consistent with previous measurements with an astrometric accuracy of $2''$ (Becker et al. 1994).

2.2. High-resolution spectroscopy

2.2.1. Observations

Observations were taken with *NIRSPEC*, the cross-dispersed echelle spectrograph mounted on Keck-II, during the night of 5th May 2006. We observed stars F01 – F17, with the exception of F12 which was missed due to time constraints. F15 was re-observed in a separate observing run on 12th Aug 2006, using the same technical setup as described below. Table 1 lists the coordinates and 2MASS magnitudes of the 17 stars, as identified in FMR06. The stars’ locations are illustrated in Fig. 2.

We used the NIRSPEC-7 filter and 0.576"×24" slit. Setting the dispersion angle to 62.53°, and cross-disperser angle to 35.53°, this gave us a spectral resolution of ~17,000 in the wavelength range 1.9–2.4μm. We integrated for 20s in two nodded positions along the slit for each star. We observed the B0V star HD 171305 as a telluric standard. We used a continuum lamp to obtain flat-field frames, while for wavelength calibration, we observed Ar, Ne, Xe and Kr lamps to obtain as many spectral lines as possible in the narrow wavelength range. To sample the gaps between these lines, we also observed the continuum lamp through an etalon filter.

2.2.2. Data reduction

To remove sky emission, dark current and bias level, we subtracted nod pairs of spectra. Fluctuations in pixel-to-pixel sensitivity were corrected for by dividing through by the normalized flat-field frame.

The optics of *NIRSPEC* produce spectral orders which are warped in both the spatial and dispersion directions, and before the spectra can be extracted this warping must be corrected for in a process known as *rectification*. The methodology we use is the same as that in DFK07, and is explained in more detail in Figer et al. (2003). Here we give a brief summary.

Spatial rectification is done by adding nod-pair spectra and fitting the spectral traces with a polynomial. Rectification in the dispersion direction is more complicated; it involves obtaining accurate wavelengths of the etalon lines using the arc frames, and assuming that the wavelength of the n th order etalon-line λ_n is governed by the separation of the etalon plates t via the relation $\lambda_n = t/2n$ (the *etalon equation*).

The arc lines were used to get initial estimates of the etalon-line wavelengths, and hence

of the etalon plate separation. The etalon-line wavelengths were then recomputed using the etalon equation, and used to re-estimate the wavelengths of the arc lines. The etalon thickness was fine-tuned in an iterative process until the residuals between the measured and predicted arc-line wavelengths across all orders were minimized.

After rectification, the spectra were extracted from each frame by summing the pixels across the trace in each channel. Shifts between spectra of up to 4 km s^{-1} ($\lesssim 1$ pixel), caused by the star not being quite in the centre of the slit, were corrected for by cross-correlating the atmospheric CO_2 feature at $2.05 \mu\text{m}$ in each spectrum.

The accuracy of the final wavelength solution is determined from the residuals between the observed and predicted arc-line wavelengths in the etalon-fitting process described above, and is better than $\pm 4 \text{ km s}^{-1}$. The internal error between spectra, from the CO_2 telluric feature, is $\ll 1 \text{ km s}^{-1}$, and so is dominated by systematics in our analysis process which we estimate to be $\pm 1 \text{ km s}^{-1}$ (DFK07).

3. Results & analysis

3.1. The maser source OH25.25-0.16

As mentioned in Sect. 1, the 1612MHz OH maser forms in the outflows of RSGs, far above the stellar surface. The velocity profiles are therefore typically doubly-peaked, with a separation twice the terminal velocity of the outflow centred on the star’s systemic velocity. However, when observed by Blommaert et al. (1994), OH25.25-0.16 appeared only as a single peak with a radial velocity $v_{\text{LSR}} = 102.2 \text{ km s}^{-1}$.

Our new observation of the OH maser source is shown in velocity-space in Fig. 1. Here it can be seen that we clearly detect the second peak. The flux-weighted mean velocities of the two peaks are $103.8 \pm 0.1 \text{ km s}^{-1}$ and $138.1 \pm 0.9 \text{ km s}^{-1}$, calculated using all channels with emission greater than 5σ above the background. The average velocity of the peaks is $120.9 \pm 0.9 \text{ km s}^{-1}$, consistent with the average velocities of the SiO masers in the cluster, $120.7 \pm 3.2 \text{ km s}^{-1}$, observed by Nakashima & Deguchi (2006). The implied outflow speed is $17.1 \pm 0.6 \text{ km s}^{-1}$, a typical outflow speed for RSGs (Richards & Yates 1998), and similar to the outflow speed of S Per ($\sim 16 \text{ km s}^{-1}$ Diamond et al. 1987), which occupies a similar location in the HR-diagram as the stars of RSGC1 (Gahm & Hultqvist 1976, see Sect. 4).

In Fig. 2 we overlay a contour plot of the 1612MHz emission on the 2MASS K_S -band image of the cluster. We find the positional centroid of the OH maser to be $18^{\text{h}}37^{\text{m}}58.882^{\text{s}}$, $-06^{\circ}52'32.28''$ (J2000), with a positional uncertainty of $0.3''$. The J2000 position of the

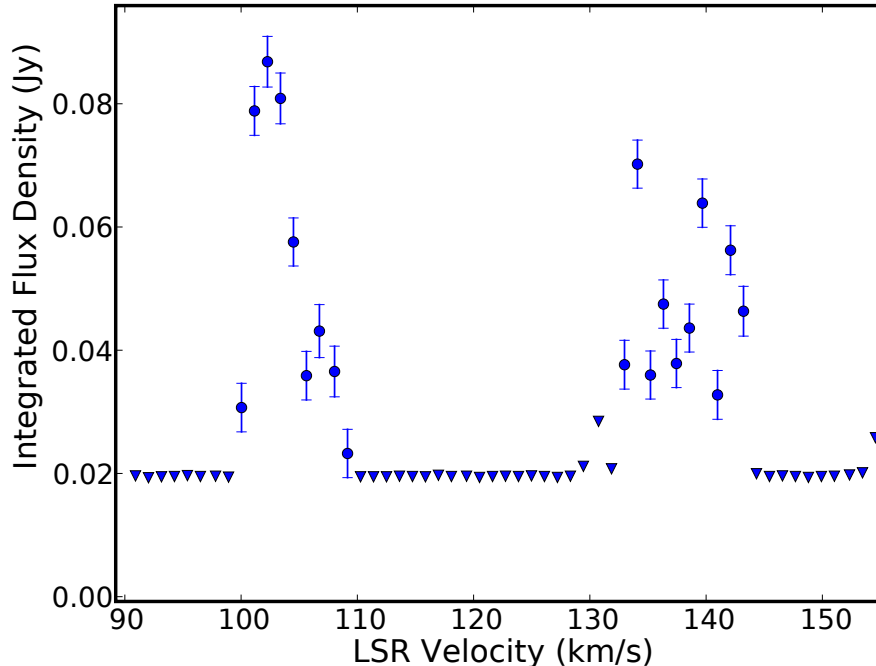


Fig. 1.—: Spectrum at 1612MHz of the source OH25.25-0.16. Our new observations clearly show the second peak at $\sim 135 \text{ km s}^{-1}$. Errorbars show $\pm 1\sigma$ uncertainty and triangles show 5σ upper limits in the flux density.

maser is consistent with previous measurement by Blommaert et al. (1994), which had a positional accuracy of $4''$. The maser is also spatially coincident with star F13, whose 2MASS coordinates are $18^{\text{h}}37^{\text{m}}58.908^{\text{s}}$, $-06^{\circ}52'32.11''$ (J2000), with positional uncertainty $0.06''$.

The central radial velocity of the OH maser is also consistent with the SiO observation of F13 by Nakashima & Deguchi (2006)², $v_{\text{LSR},\text{F13}} = 120.5 \pm 2.0 \text{ km s}^{-1}$, and with the CO-bandhead radial velocity measurement of F13 presented in this paper, $125.4 \pm 4 \text{ km s}^{-1}$ (see Sect. 3.2.1). From this evidence, it seems highly likely that the OH maser originates in the outflow of F13.

In addition to the OH maser, we also detect the continuum sources GPSR5 (25.266-0.161, 25.252-0.139, 25.237-0.15). These sources were shown conclusively to be extragalactic in origin by Trejo & Rodríguez (2006).

²This radial velocity was found from the average velocity of the high- and low-velocity edges. The centroid of the peak of this source was found to have a radial velocity of $116.5 \pm 2 \text{ km s}^{-1}$

Table 2:: Observed data for RSGs. (1): the stellar IDs (from FMR06); (2): the radial velocity of each star ($\pm 4 \text{ km s}^{-1}$), and the radial velocity measured by Nakashima & Deguchi (2006), where available ($\pm 2 \text{ km s}^{-1}$); (3): effective temperature; (4): spectral type, accurate to ± 2 subtypes; (5) derived extinction towards each star; (6): absolute K -band magnitude; and (7): bolometric luminosity.

(1)	(2)	(3)	(4)	(5)	(6)	(7)	
ID	V_{LSR} (km s^{-1})	(ND06) ¹ T_{eff} (K)	Spec Type	A_{K_S}	M_K	$\log(L_{\text{bol}}/L_{\odot})$	
F01	129.5	(117.7)	3450 \pm 127	M5	2.58 \pm 0.09	-11.75 $^{+0.34}_{-0.30}$	5.42 $^{+0.12}_{-0.13}$
F02	114.2	(119.7)	3660 \pm 127	M2	2.83 \pm 0.07	-11.92 $^{+0.34}_{-0.30}$	5.56 $^{+0.12}_{-0.13}$
F03	127.2	–	3450 \pm 127	M5	2.46 \pm 0.09	-11.28 $^{+0.34}_{-0.30}$	5.24 $^{+0.12}_{-0.13}$
F04	121.2	(124.3)	3752 \pm 117	M1	2.46 \pm 0.04	-11.24 $^{+0.32}_{-0.28}$	5.32 $^{+0.11}_{-0.13}$
F05	124.8	–	3535 \pm 130	M4	2.77 \pm 0.08	-11.36 $^{+0.34}_{-0.30}$	5.29 $^{+0.12}_{-0.14}$
F06	120.7	–	3450 \pm 127	M5	2.19 \pm 0.09	-10.70 $^{+0.34}_{-0.30}$	5.00 $^{+0.12}_{-0.13}$
F07	121.6	–	3605 \pm 151	M3	2.33 \pm 0.12	-10.81 $^{+0.36}_{-0.32}$	5.10 $^{+0.13}_{-0.14}$
F08	128.2	–	3605 \pm 151	M3	2.84 \pm 0.12	-11.33 $^{+0.36}_{-0.32}$	5.30 $^{+0.13}_{-0.14}$
F09	121.6	–	3399 \pm 150	M6	2.44 \pm 0.08	-10.92 $^{+0.33}_{-0.29}$	5.07 $^{+0.12}_{-0.13}$
F10	122.0	–	3605 \pm 151	M3	2.45 \pm 0.12	-10.86 $^{+0.36}_{-0.32}$	5.12 $^{+0.13}_{-0.14}$
F11	124.1	–	3535 \pm 130	M4	2.63 \pm 0.08	-11.03 $^{+0.34}_{-0.30}$	5.16 $^{+0.12}_{-0.14}$
F13	125.4	(120.5)	4015 \pm 140	K2	3.19 \pm 0.09	-11.39 $^{+0.34}_{-0.30}$	5.45 $^{+0.12}_{-0.13}$
F14	122.0	–	3605 \pm 151	M3	2.29 \pm 0.12	-10.25 $^{+0.36}_{-0.32}$	4.87 $^{+0.13}_{-0.14}$
F15	120.8	–	6850 \pm 350	G0	2.65 \pm 0.04	-10.07 $^{+0.40}_{-0.36}$	5.36 $^{+0.14}_{-0.16}$
<i>F16</i>	<i>42.6</i> ²	–	–	–	–	–	–
<i>F17</i>	<i>33.2</i> ²	–	–	–	–	–	–

¹We quote the Nakashima & Deguchi (2006) values measured by taking the average of the high- and low-velocity edges of the maser profiles.

²Stars F16 & F17 are determined to be foreground stars, and due to the uncertainties in reddening and distance we derive no stellar parameters for these stars.

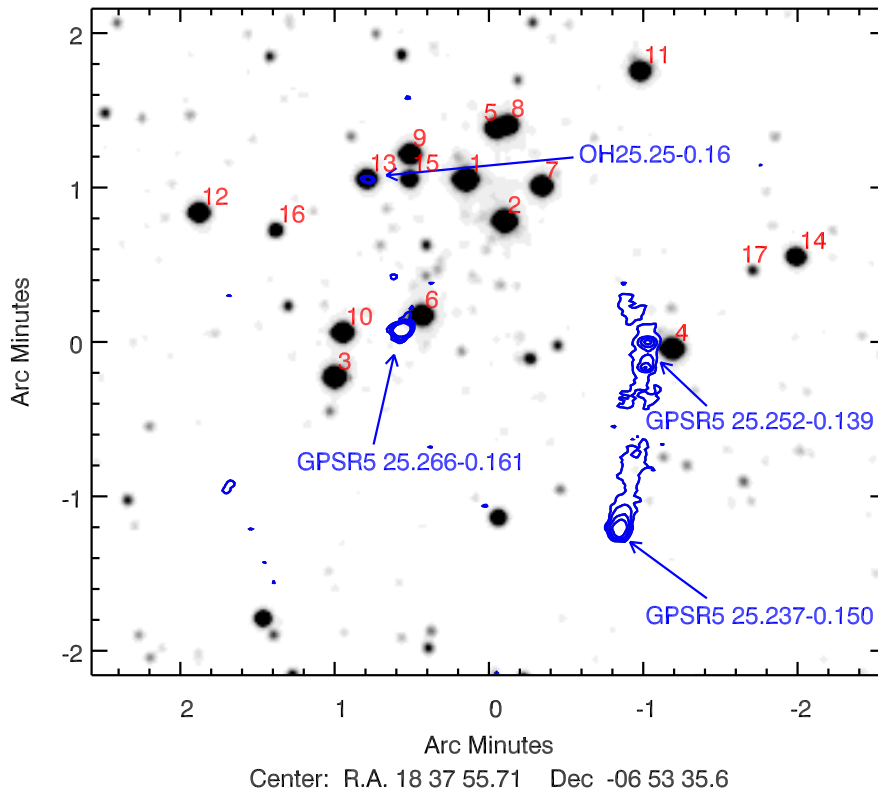


Fig. 2.—: Contour-plot of the 1612Hz radio image, overlaid on the 2MASS K_S -band image of the same region. The image is centered on the indicated coordinates (epoch J2000). Contours are drawn at 5, 10, 20 and 40σ above the background; the 1σ level corresponds to 0.87mJy/beam. The position of the OH maser is indicated, and is coincident with star F13. The other identified radio sources in the field, labelled in the figure, were shown by Trejo & Rodríguez (2006) to be extragalactic in origin. The stars F01 to F17, as designated by FMR06, are also labelled.

3.2. The high-resolution spectra

The high-resolution observations of the region around the CO-bandhead feature at $2.293\mu\text{m}$ for the 17 K-bright stars are shown in Fig. 3. All stars observed, with the exception of F15, show the feature strongly in absorption; F15 has it weakly in emission. Quantitative analysis of the high-resolution spectroscopy results are described below.

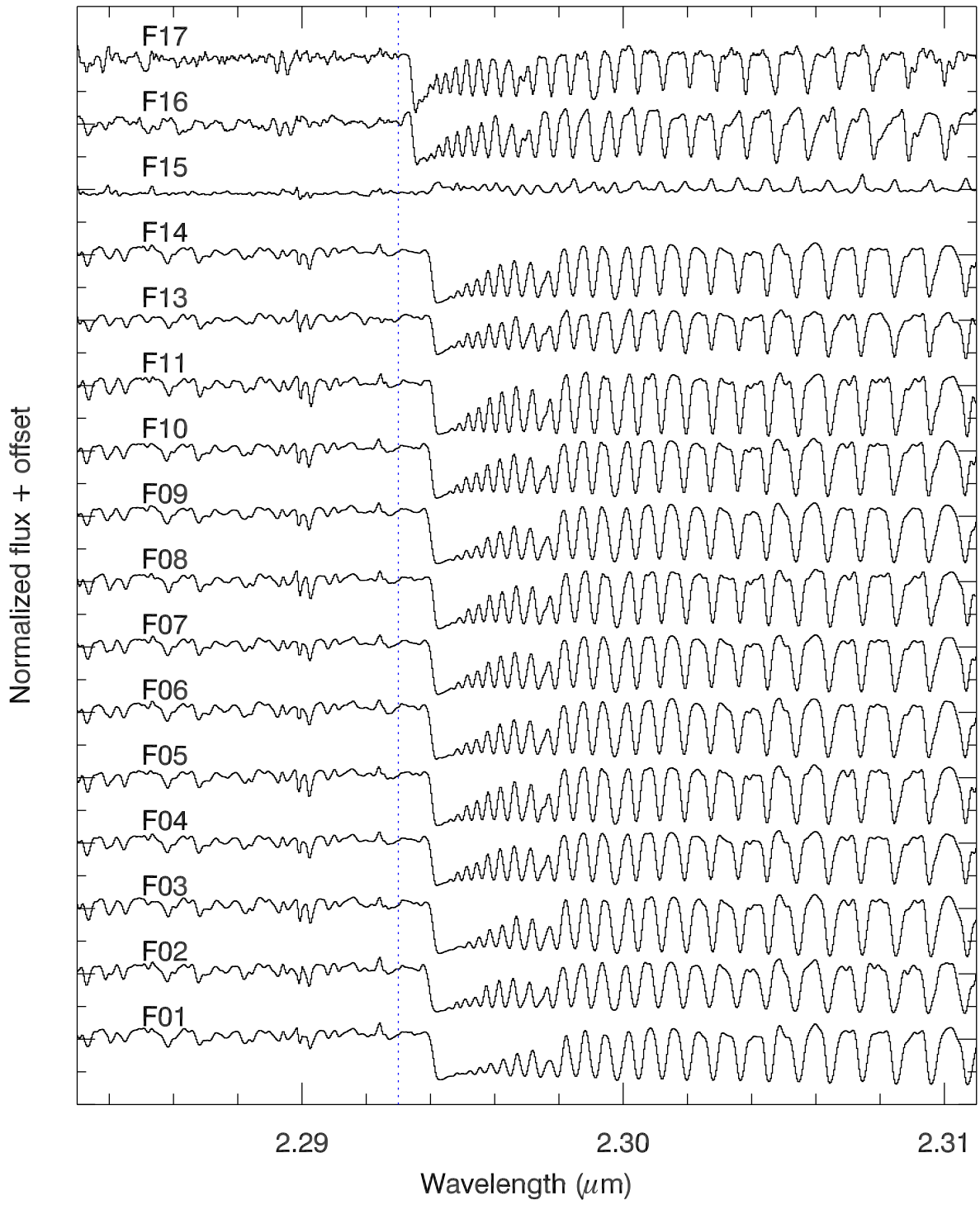


Fig. 3.—: High-resolution spectra of all stars observed in the region of the CO-bandhead feature. The dotted blue line indicates the zero velocity of the blue edge of the CO bandhead.

3.2.1. *Stellar radial velocities*

The radial velocities of each star serve two purposes; firstly they allow us to distinguish between genuine cluster stars and foreground stars with similar colours; and secondly they allow us to derive a kinematic distance to the cluster.

The differences in radial velocities of the stars can be seen qualitatively in Fig. 3 – the blue-edges of the CO bandhead in stars F16 and F17 are noticeably blue-shifted compared to stars F01 – F15, which all have very similar radial velocities.

In order to accurately quantify the radial velocities of the stars, we implemented the same technique as presented in Figer et al. (2003) and DFK07. We cross-correlated the spectra shown in Fig. 3 with that of the high-resolution spectrum of Arcturus presented in Wallace & Hinkle (1996a), which had been degraded to the same spectral resolution as our data. For star F15, which has CO in emission, we inverted the spectrum before analysis. We experimented with isolating different spectral ranges during the cross-correlation, to determine the robustness of our measurements. We found that the measured velocities were stable to within $\pm 1 \text{ km s}^{-1}$, which we take to be the *internal* error between individual measurements. The absolute uncertainty on the measurements is limited by the accuracy of the wavelength solution, $\pm 4 \text{ km s}^{-1}$ (see Sect. 2).

We find that stars F01 – F15 all have radial velocities in the range $v_{\text{LSR}} \sim 115\text{-}125 \text{ km s}^{-1}$, while stars F16 and F17 have v_{LSR} of 33 km s^{-1} and 43 km s^{-1} respectively. From this, we conclude that the two faintest stars observed are foreground stars, while stars F01 – F15 are physical members of the cluster. As F12 was unobserved, the status of this star is still unclear. We note that the CO absorption strengths of stars F16 and F17 are much lower than those of the RSGs, and instead are more typical of less luminous stars. This is consistent with these stars being foreground objects.

The measured radial velocities of all stars observed are listed in Table 2. Also listed in Table 2, where available, are the radial velocities determined from SiO maser emission by Nakashima & Deguchi (2006). We see that the two measurements of stars F02, F04 and F13 are within $\sim 2\sigma$, while for F01 it is $\sim 3\sigma$. As SiO masers are commonly thought to trace the stellar systemic velocity (Jewell et al. 1991), we would expect the two velocity measurements to agree well. However, we note that the observations of Nakashima & Deguchi (2006) may have been hampered by their beam-size; their observations of F01, F02 and F13 have at least one other RSG within the beam FWHM. In the case of F04, which is well separated from the other RSGs, the CO bandhead and SiO maser measurements are in excellent agreement. As mentioned in Sect. 3.1, the measured radial velocity of F13 is in excellent agreement with observations of the OH and SiO maser sources at the same location.

3.2.2. Distance to RSGC1

We take the mean radial velocity of the stars observed at high spectral resolution and compare with the Galactic rotation curve, using the contemporary measurements collated by Kothes & Dougherty (2007). The mean radial velocity of the stars from the CO observations is $123.0 \pm 1.0 \text{ km s}^{-1}$, with an uncertainty determined from Poisson statistics of the measurements. The absolute uncertainty on the radial velocity is therefore dominated by that in the wavelength solution, $\pm 4 \text{ km s}^{-1}$. This compares well to the average radial velocity found by Nakashima & Deguchi (2006), $\sim 120 \pm 2 \text{ km s}^{-1}$, from their SiO maser observations³, and the central velocity of our new 1612MHz OH maser observation, $120.9 \pm 0.9 \text{ km s}^{-1}$.

In Fig. 4 we compare our radial velocity to the Galactic rotation curve in the direction of $l = 25.15^\circ$, $b = -0.15^\circ$. We use the distance to the Galactic centre $D_{\text{GAL}} = 7.5 \pm 0.3 \text{ kpc}$ (Eisenhauer et al. 2005), and solar rotational velocity $\Theta_{\odot} = 214 \pm 7 \text{ km s}^{-1}$ (Feast & Whitelock 1997; Reid & Brunthaler 2004). We use the uncertainties on these values to construct ‘maximal’ and ‘minimal’ rotation curves in Fig. 4.

The cluster radial velocity actually extends beyond the asymptotic point of the curve; however it lies well within the two ‘error’ curves, and therefore could simply be due to the uncertainties in D_{GAL} and Θ_{\odot} . To determine the distance to the cluster, we take the average of the two points where the radial velocity intercepts the ‘maximal’ rotation curve. This gives us a kinematic distance to the cluster of $6.60 \pm 0.89 \text{ kpc}$, slightly larger than the distance quoted in FMR06 when using the radial velocity of the singly-peaked OH maser.

3.2.3. Effective temperatures

To determine the spectral-types of the RSGs, and hence their effective temperatures, we used the same empirical method described in Davies et al. (2007). We compared the equivalent width (W_{λ}) of the CO bandhead absorption with that of template stars, taken from the catalogues of Kleinmann & Hall (1986), Wallace & Hinkle (1996b) and Wallace & Hinkle (1997). We defined a measurement region of $2.294\text{--}2.304 \mu\text{m}$, and defined the continuum as the median of the range $2.288\text{--}2.293 \mu\text{m}$. We estimated the uncertainty by repeating the measurements with slightly adjusted continuum regions, and found that measurements were stable to $\sim 1 \text{ \AA}$, or $\sim 5\%$. To find the spectral-types of the RSGs, we compared the W_{λ} measurements with a linear fit to the W_{λ} of the template stars as a function of spectral-

³These values are the average of their two different methods of measuring the radial velocity of each star from the maser line profile

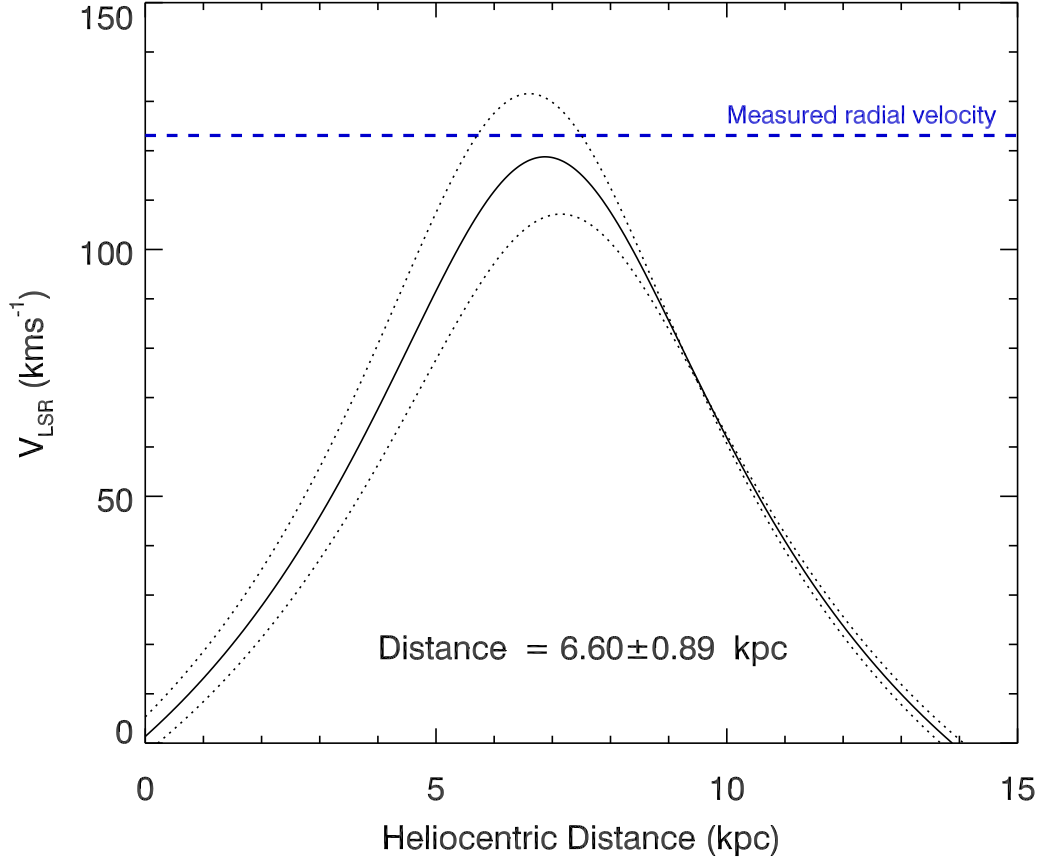


Fig. 4.—: Galactic rotation curve in the direction of RSGC1 (Brand & Blitz 1993), using the measurements of collated by Kothes & Dougherty (2007).

type. Using this method, we are able to determine spectral-types to within ± 2 subtypes (see DFK07). In converting spectral-type to effective temperature, we used the temperature scale of Levesque et al. (2005). The derived spectral-types and effective temperatures for the RSGs are listed in Table 2.

For star F15 the method described above breaks down, as this star has CO in emission. The star’s radial velocity suggests that it is part of the cluster, and hence a supergiant. It was assigned the spectral-type G6 I in FMR06, and hence deemed to be a ‘Yellow Hypergiant’ (YHG), based on its weak CO-bandhead absorption. Given that this was only a marginal detection of CO absorption here we reappraise the star’s spectral type.

Figure 5 shows the spectra of F15 on the two occasions it was observed. It can be seen that the CO-bandhead, which was present in emission in May, was not detected at all in August. Over the rest of the star’s spectrum, no discernable variability is observed.

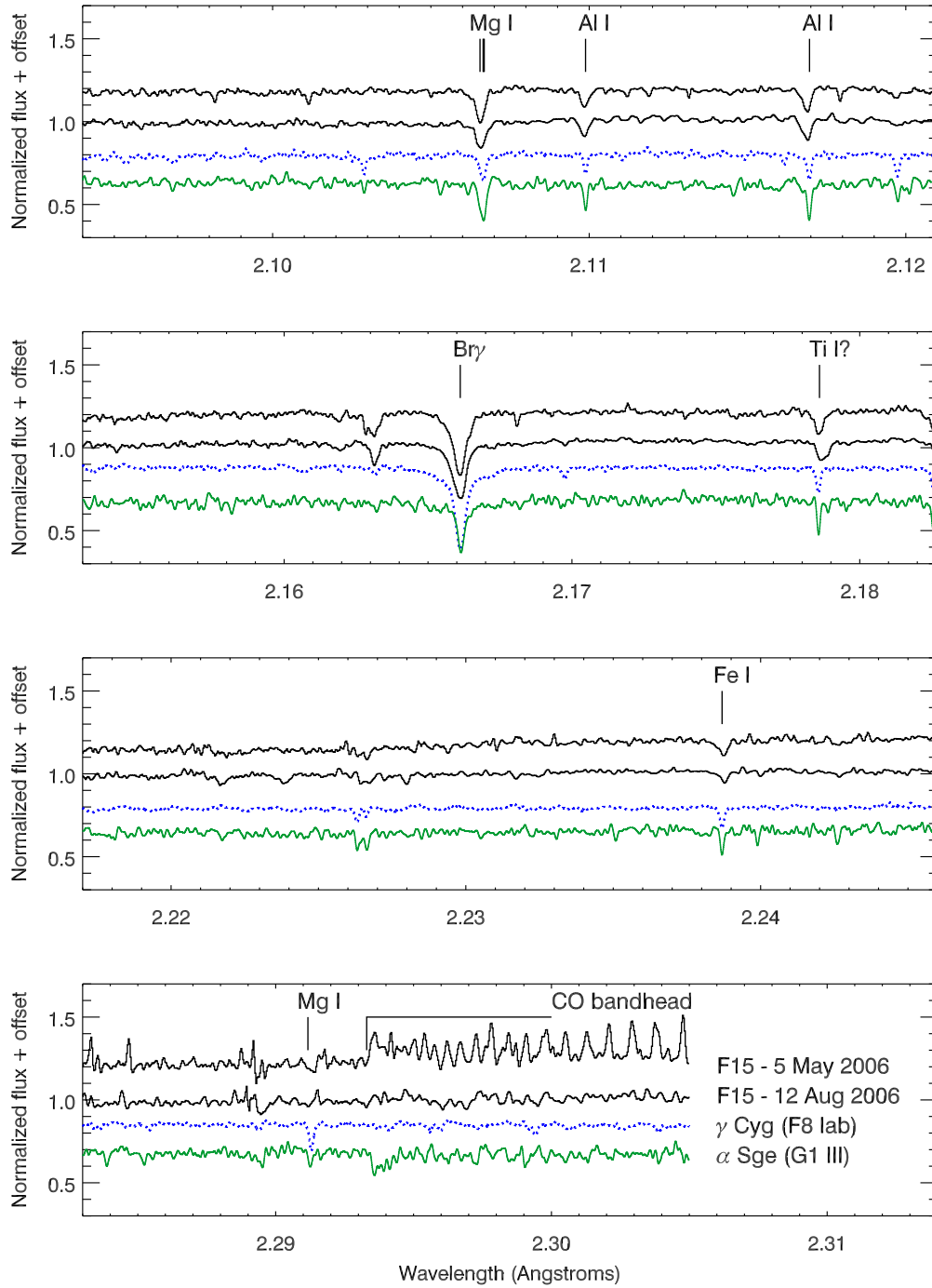


Fig. 5.—: The high-resolution K-band spectrum of F15, compared to the spectra of γ Cyg and α Sge from Wallace & Hinkle (1997).

For comparison, Fig. 5 shows similar template spectra of γ Cyg, spectral-type F8 Iab, and α Sge, spectral-type G1 III, which have been resampled to the same spectral resolution as our data (taken from Wallace & Hinkle 1997). Though admittedly α Sge has a lower luminosity class than that inferred for F15, it serves to give some insight into F15’s temperature. At spectral-type G1, the CO-bandhead absorption is still seen, albeit weakly. The star also shows the atomic absorption lines of Al I, Fe I, Mg I, and Br γ . However, at this temperature molecular absorption, mostly from CN, can be seen as the undulating ‘noise’-like features throughout the spectrum. At spectral-type F8, the CN and CO absorption are gone, while the atomic absorption lines remain.

From these comparison spectra, we assign a spectral-type to F15 of G0, ± 2 subtypes, and hence an effective temperature of $T_{\text{eff}} = 6500 - 7200\text{K}$. Indeed, the star is very similar spectroscopically to ρ Cas, one of the archetypal YHGs, which also shows transient CO emission / absorption (see spectra presented in Gorlova et al. 2006).

3.2.4. Extinction

The extinction towards each star is measured by comparing the 2MASS infrared colours of the stars to the intrinsic colours of supergiants with the same spectral-type. For the RSGs we use the observations of Galactic stars with luminosity class Iab from Elias et al. (1985); while for F15 (the YHG) we use the tables of Koornneef (1983). We define the excess between the observed and intrinsic colours as the reddening towards each star. We convert this reddening to an extinction towards each star using the relationship of Rieke & Lebofsky (1985),

$$A_{K_S} = \frac{E_{\lambda-K_S}}{(\lambda/\lambda_{K_S})^{1.53} - 1} \quad (1)$$

where λ is the wavelength appropriate for the 2MASS J or H filters. To determine the uncertainty in each extinction measurement we derive extinctions for the upper and lower limits to each star’s spectral-type. Where the difference between the derived $A_{K_S}(J - K_S)$ and $A_{K_S}(H - K_S)$ values is outside this uncertainty, we adopt half this difference as the error in the measurement.

Using this method, we find a median extinction of $A_{K_S}(J - K_S) = 2.58$, and $A_{K_S}(H - K_S) = 2.62$. Each have uncertainties of 0.07mags from Poisson statistics, and are therefore in good agreement with one another. We adopt the mean of these measurements, $A_{K_S} = 2.60 \pm 0.07$ as the median extinction towards the cluster. We note that the extinction towards

the YHG, $A_{K,F15} = 2.65 \pm 0.02$, is consistent with that derived for the RSGs.

The median cluster extinction is slightly lower than the $A_{K_S} = 2.74 \pm 0.02$ derived in FMR06. We consider the latest measurement to be the more reliable, due to the extra assumptions used in FMR06: instead of dereddening each star according to the intrinsic colours appropriate for its spectral-type, they dereddened *all* stars to the mean colour of M supergiants from Elias et al. (1985). The ranges in colours of M supergiants are $\Delta(J - K) \sim 0.3$ and $\Delta(H - K) \sim 0.1$, which each correspond to $\Delta A_{K_S} \sim 0.2$ using Eqn. (1). Hence, if the spectral-types of the RSGs are asymmetrically distributed about the mean spectral-type, this may produce a derived extinction out by as much as 0.2, consistent with the difference between the extinctions derived here and in FMR06.

3.2.5. Luminosities

We take the extinctions toward each star derived in Sect. 3.2.4, in conjunction with the distance to the cluster estimated in Sect. 3.2.2 to determine the absolute K_S -band magnitudes of the stars. To convert these to bolometric luminosities (L_\star) we interpolate over the contemporary bolometric corrections BC_K for RSGs, given in Levesque et al. (2005), for the stellar temperatures derived in Sect. 3.2.3.

The absolute uncertainty in each L_\star determination is $\sqrt{(\delta A_K + \delta BC_K + \delta D_{cl})}$. As we can confidently make the approximation that all the stars are all located at the same distance, the uncertainty in distance (δD_{cl}) can be neglected when analysing the luminosity spread of the stars to infer the cluster’s age (see Sect. 4.1). The uncertainties in both A_K and BC_K are carried forward from the error in T_{eff} , and are determined by substituting the upper and lower limits to the stars’ temperatures.

We list the stars’ luminosities in Table 2, along with uncertainties which include the error in the cluster distance. The newly-derived values are similar to those quoted in FMR06, typically within $\pm 0.3\text{dex}$. As stated above, FMR06 used the same extinction towards all stars in the cluster, an approximation which breaks down if there are large variations in the interstellar extinction across the field or if a star has extra circumstellar extinction. Also, our high S/N, high-resolution spectra give a more accurate picture of variations in CO equivalent width, and hence better constrained stellar temperatures – key in evaluating the stars’ bolometric corrections. For these reasons, we conclude the bolometric luminosities derived here to be the more accurate than those quoted in FMR06.

3.2.6. Spectral energy distributions

Using the Galactic plane surveys of MSX and GLIMPSE (Egan et al. 2001; Benjamin et al. 2003), as well as 2MASS, we have collated IR photometry for all stars observed here. For the brighter stars, mid-IR photometry is unavailable due to the stars saturating in the images (e.g. F01 and F02); while fainter stars in crowded regions (e.g. F15) are dwarfed by brighter nearby stars (e.g. F09). We rejected all upper-limit measurements and all detections fainter than 10σ .

In Fig. 6 we plot the spectral energy distribution (SED) of each star. Also plotted in the figure are the stars’ de-reddened photometry, which were calculated using the interstellar extinction toward each star in conjunction with the extinction-laws quoted by Indebetouw et al. (2005) and Messineo et al. (2005). We have overplotted blackbody curves appropriate for the stellar temperatures and luminosities calculated in Sects. 3.2.3 and 3.2.5.

In all cases, the blackbodies provide excellent fits to the near-IR photometry, even in the case of F15 where a less accurate method of temperature estimation was possible. This serves to validate the stellar luminosities and temperatures of the stars derived above (c.f. Fig. 13 of FMR06, where poorer fits to the IR photometry were obtained.).

In all cases where photometry is available, the mid-IR MSX data shows that the stars have considerable excess emission. This is indicative of warm circumstellar dust, a product of the high mass-loss rates of the stars. Also, the SEDs appear to show bumps around $12\mu\text{m}$, which can be understood as silicate emission from the oxygen-rich dust. A detailed study of the circumstellar material around these objects will be the subject of a future paper.

4. Discussion

4.1. Cluster age

In Fig. 7, we plot the derived temperatures and luminosities of the cool, luminous stars on a H-R diagram. Also plotted are isochrones taken from the stellar evolutionary models of Meynet & Maeder (2000) which include the effects of rotation, and have initial rotational velocity set to 300 km s^{-1} . As we can confidently make the approximation that all the stars are at the same distance, we do not include the error in distance on each data-point. The magnitude of the error in L_\star when this uncertainty *is* included is shown on the right of the plot.

The figure shows that the temperatures and luminosity spread of the RSGs are well-

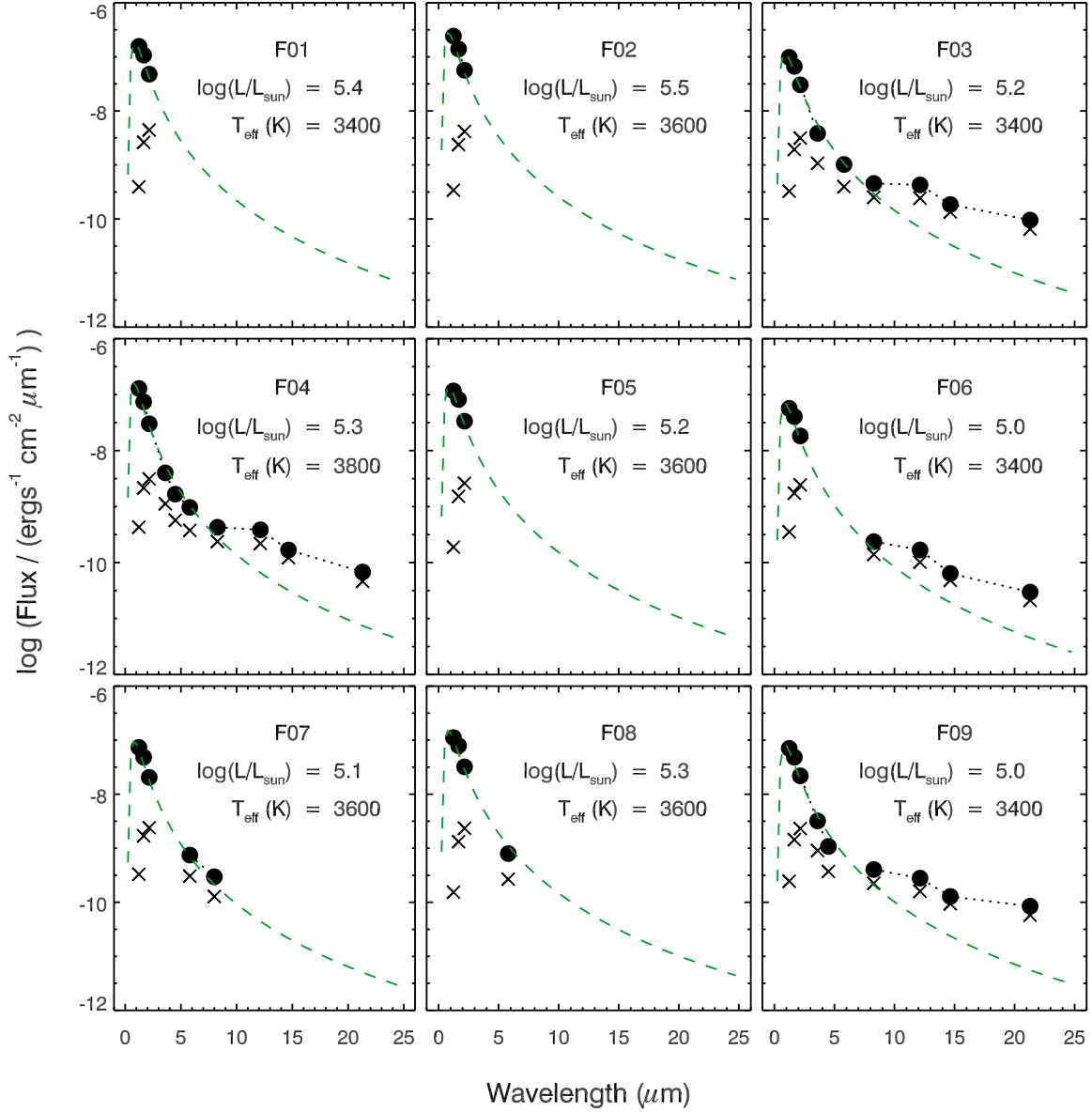


Fig. 6.—: Spectral energy distributions of cluster members. Crosses are raw photometry from 2MASS, GLIMPSE & MSX; filled circles are dereddened according to the stellar extinctions derived in Sect. 3.2.4. Over plotted in green is a black-body curve, with T determined from spectral-type of star and luminosity according to dereddened K-band magnitude at a distance of 5.88kpc.

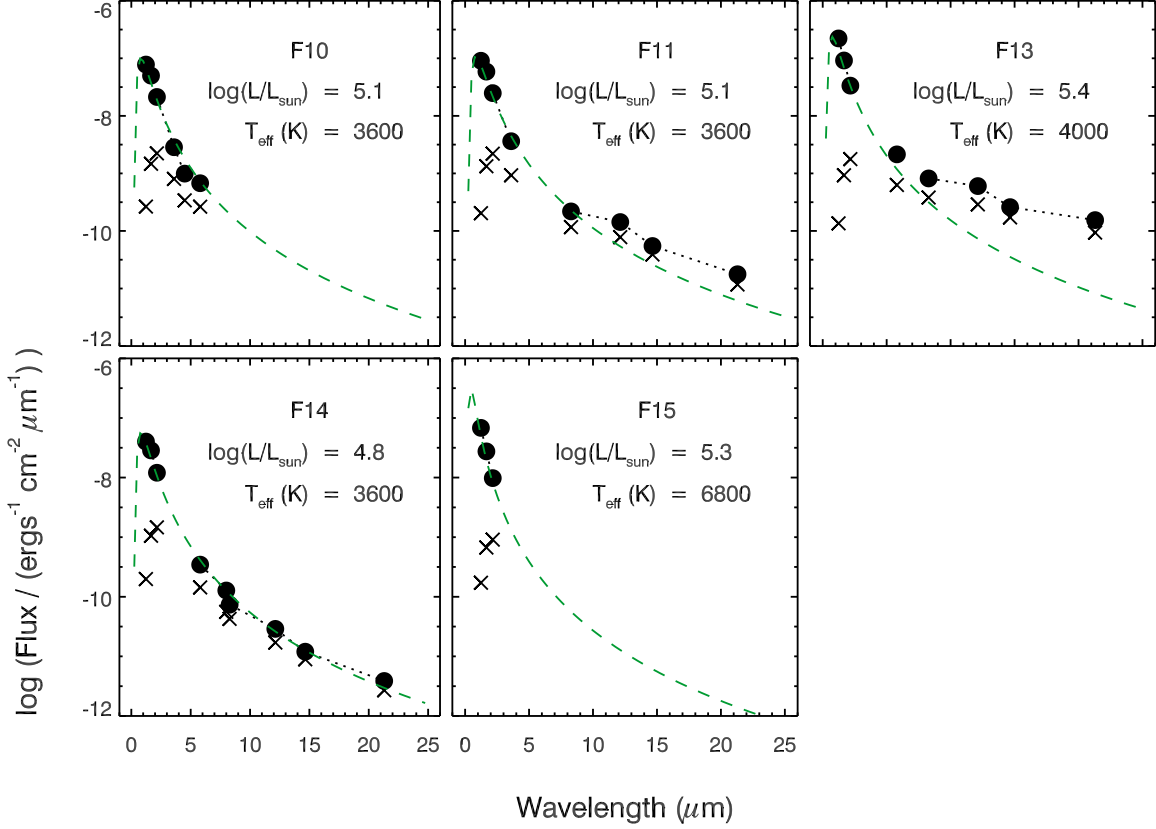


Fig. 6.—: Cont.

matched by the 12Myr isochrone. The 10Myr isochrone cannot reproduce the low-luminosity stars, while the 14Myr isochrone is too faint to fit the high-luminosity stars. When the uncertainty in cluster distance is taken into account (ΔD_{cl} in Fig. 7), the 10Myr and 14Myr isochrones appear more reasonable. We experimented with different evolutionary models, namely non-rotating models with varying mass-loss rates and metallicity (Schaller et al. 1992; Schaerer et al. 1993; Meynet et al. 1994). We found generally that the non-rotating models gave ages that were $\lesssim 2$ Myr younger. We settle on an age estimate for RSGC1 of 12 ± 2 Myr.

We note that the YHG F15 does *not* lie on the 12Myr isochrone in Fig. 7. Fitting the star with the rotating Geneva isochrones, we get an age of 10Myr (pre blue-loop) or 8Myr (post blue-loop). For the specific models used in this analysis, the masses of RSGs in a 12Myr-old cluster do not experience a blue-loop. However, the specific masses of stars which experience blue-loops are extremely sensitive to the input physics, such as rotation (see Fig. 1 of Hirschi et al. 2004). Hence, a blue-loop may be introduced for stellar initial

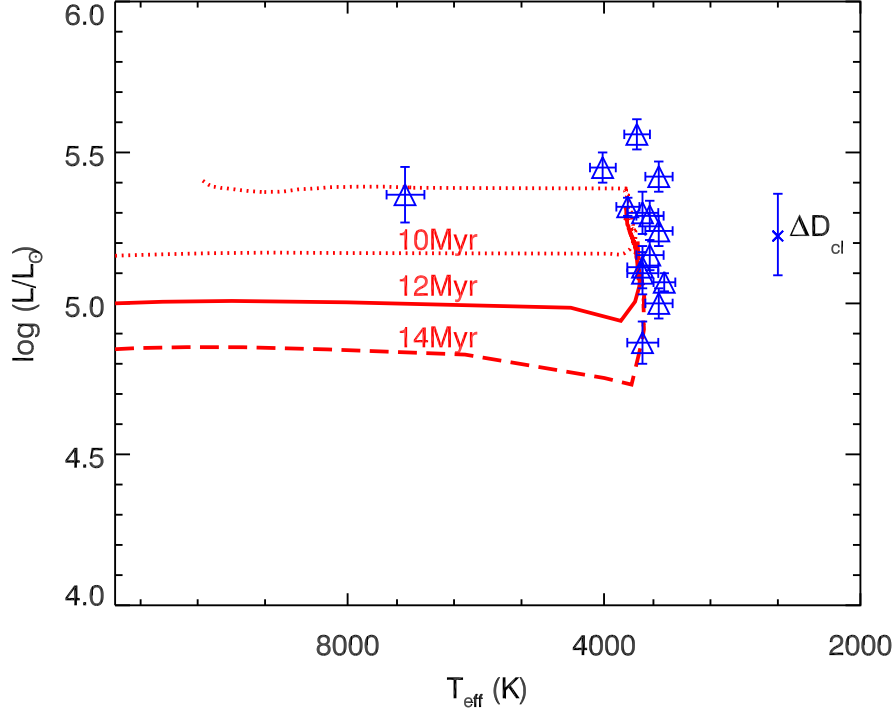


Fig. 7.—: H-R diagram, showing the location of the RSGs and one YHG. Overplotted are rotating Geneva isochrones from Meynet & Maeder (2000), with ages 10, 12 and 14 Myr. The luminosity spread of the RSGs is well-matched by the 12Myr isochrone. Errors on the data-points do not include the uncertainty in cluster distance ΔD_{cl} – the magnitude of this error is indicated at the right of the plot. The data-point separated from the rest is the YHG F15.

masses relevant to RSGC1 simply by changing the rotational speed. Additionally, it is likely that blue-loops would be affected by the inclusion of extra physics (e.g. magnetic fields). In summary, We do not necessarily interpret F15’s location in the H-R diagram as evidence of cluster non-coevality, it could simply be that the input physics of the evolutionary models used in the analysis are not fine-tuned to this cluster.

If the RSGs of this cluster do experience some form of blue-loop, then the position of F15 on the H-R diagram is consistent with it evolving *away* from the RSGs. A post-RSG nature for this star would make it a member of a very exclusive club – arguably IRC +10420 is the only object which is widely accepted to be a post-RSG, though a case has also been argued for HD 179821 (see review of Oudmaijer et al. 2008). We note that F15 does not exhibit the same considerable IR excess, nor the bright maser emission of IRC +10420. This may be due to F15’s lower initial mass – the Geneva models imply $\sim 18M_{\odot}$ for F15, while the larger luminosity of IRC +10420 makes it consistent with a star of initial mass $\sim 40M_{\odot}$.

(see also Sect. 4.4).

The cluster age we derive is slightly greater than the age of $\lesssim 9$ Myr derived in FMR06. This previous estimate was determined by comparing the luminosity spread of the RSGs to that predicted by the non-rotating isochrones of Schaller et al. (1992) as a function of age. The more rigorous investigation of the stars’ luminosities in this present paper results in a larger luminosity spread for the RSGs, while the non-rotating models do not reproduce the higher luminosities. Much better agreement is found between the contemporary rotating models and the new luminosity estimates.

Finally, we remark that the observed temperatures of the stars are systematically cooler than the isochrones (see also Fig. 11). This could be reconciled by increasing either the relative metal abundances or the stellar rotational velocities. Both lead to slightly increased stellar radii, the former due to the increased opacity of the envelope, the latter due to the lower effective gravities. A super-solar metallicity would certainly be consistent with the Galactic metallicity gradient and the cluster’s Galacto-centric distance (~ 3 kpc). However, given the well-known disparities between observations and theory in the field of RSGs, we attach a cautionary note to any conclusions derived from this evidence. While recent progress has been made in uniting theory and observation at solar metallicity (Levesque et al. 2005), discrepancies still exist at sub-solar metallicities (Levesque et al. 2006). The location in the Galaxy of the Scutum clusters would seem to make non-solar metallicities likely. Accurate abundance measurements of the clusters would make them ideal testbeds for evolutionary models, as well as probes of the Galactic metallicity gradient.

4.2. Cluster mass

To determine the cluster mass we employ the same Monte-Carlo technique used in FMR06 and DFK07. We generate a synthetic cluster of a pre-defined initial mass, containing stars whose masses are randomly drawn from a distribution consistent with a Salpeter initial mass function (Salpeter 1955). Then, for a given cluster age, we determine the present-day masses, temperatures and luminosities from the Geneva isochrones used in Sect. 4.1. We then count the number of RSGs in the cluster, where we define a RSG as a star whose temperature is lower than 4000K and luminosity greater than $10^4 L_{\odot}$. As this is a random process, we repeat each simulation 1000 times to reduce statistical noise.

In Fig. 8, we plot the number of RSGs contained in a synthetic cluster as a function of cluster age, for two initial cluster masses: $20,000 M_{\odot}$ and $40,000 M_{\odot}$. The plot shows that significant numbers of RSGs begin to be seen after ~ 7 Myr – in clusters younger than

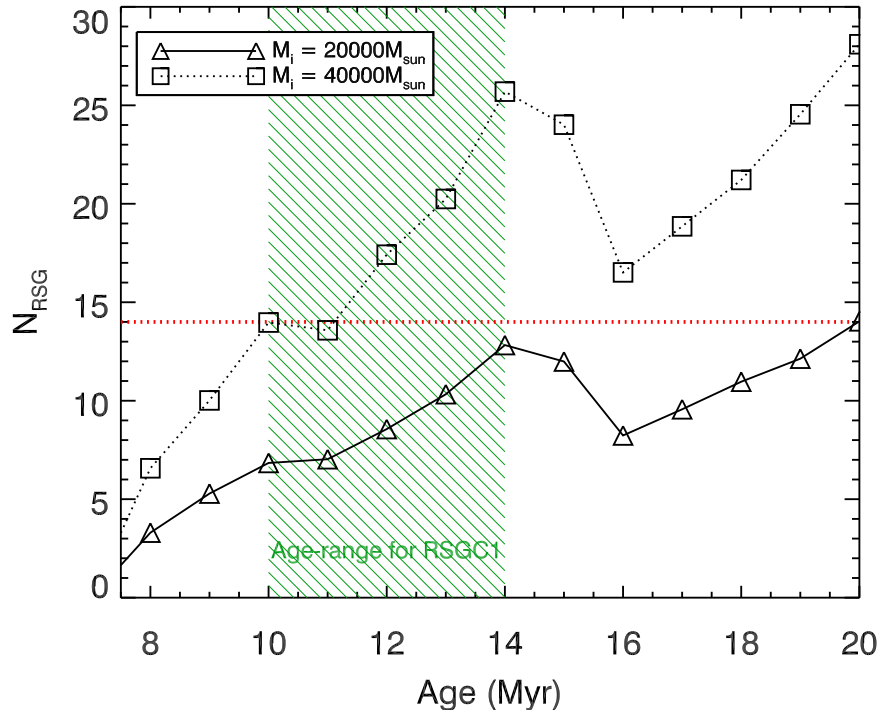


Fig. 8.—: The number of RSGs as a function of age for a coeval cluster of a given initial mass, calculated using the rotating Geneva isochrones (Meynet & Maeder 2000). The age-range for RSGC1, determined from isochrone fitting, is indicated on the plot, as is the number of RSGs observed in the cluster.

this the post-MS stars are massive enough to evolve directly to the WN phase, skipping the RSG stage. Peaks in the number of RSGs are reached at ~ 14 Myr and ~ 20 Myr, the dip in between is caused by the onset of a blue-loop in the stars’ evolution for a narrow range of initial masses. The mean luminosity of the RSGs as a function of time decreases, as the initial masses of the stars in the RSG zone becomes smaller (see Fig. 7, and discussion in Sect. 4.3). For a cluster containing 14 RSGs with an inferred age of 12 ± 2 Myr (see above), we find that the initial mass of the cluster must be somewhere in between these two, implying an initial mass of RSGC1 of $(3 \pm 1) \times 10^4 M_{\odot}$.

Using the velocity dispersion of the RSGs, we can compare this value of the cluster’s initial mass to the cluster’s *dynamical* mass, under the assumption that the cluster is currently in virial equilibrium. The dynamical mass M_{dyn} is derived using the relation,

$$M_{\text{dyn}} = \frac{\eta \sigma_v^2 r_{\text{hp}}}{G} \quad (2)$$

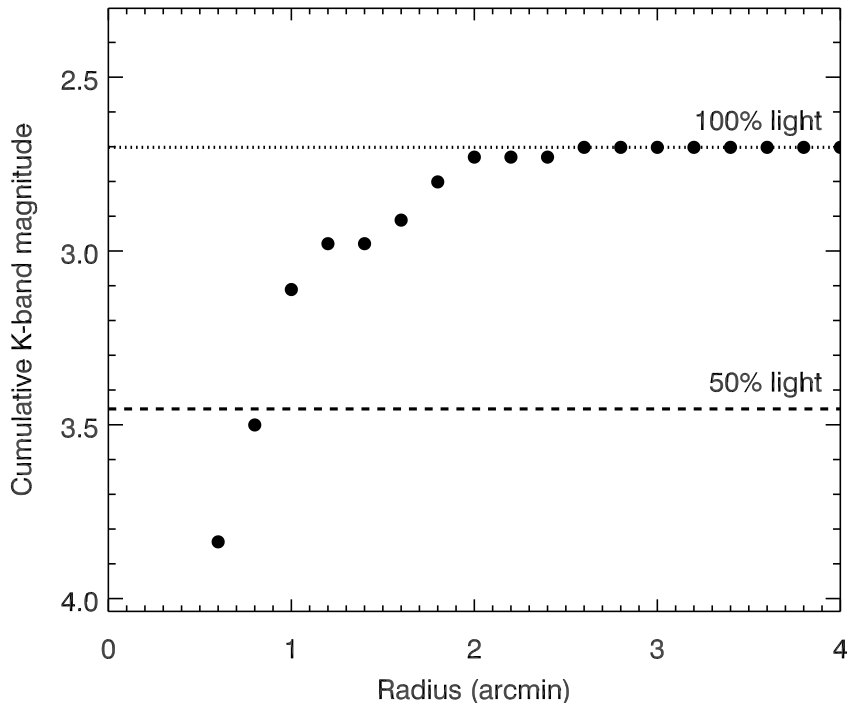


Fig. 9.—: Cumulative apparent magnitude distribution of the cluster, centred on $18^h37^m57.4^s$, $-6^\circ52'58.11''$ (J2000), using the 15 cool luminous stars as tracers of the cluster’s spatial distribution.

where r_{hp} is the half-light radius, σ_v^2 is the velocity dispersion, G is the gravitational constant, and η is a constant which depends on the stellar distribution with radius, and is typically taken to be ~ 10 (see review in Introduction of Mengel et al. 2002).

For the velocity dispersion, we find $\sigma_v^2 = 3.7 \text{ km s}^{-1}$ after the internal uncertainty in the wavelength solution ($\pm 1 \text{ km s}^{-1}$) has been subtracted in quadrature. To find the half-light radius, we plot the cumulative brightness profile of the cluster using stars F01–15 as tracers of the cluster’s spatial distribution (see Fig. 9). We used a cluster centre of $18^h37^m57.4^s$, $-6^\circ52'58.11''$ (J2000), the approximate mid-point of the cool stars. We experimented with moving the cluster centre by up to $0.5'$, using different photometric bands, and using the luminosities derived in Sect. 3.2.5 rather than the raw photometry. From all these methods we found that the cluster half-light radius was stable at $0.8 \pm 0.1''$. At the distance derived in Sect. 3.2.2, this gives a cluster size $r_{\text{hp}} = 1.5 \pm 0.3 \text{ pc}$.

Using these values, we find the dynamical mass of RSGC1 to be $M_{\text{dyn}} = (5 \pm 1) \eta / 10 \times 10^4 M_\odot$. Due to the extra uncertainty in the density parameter η , we consider this to be an order-of-magnitude estimate only, which compares well to the initial cluster mass derived using evolutionary models.

Table 3: Properties of the two Scutum RSG clusters. (1): cluster name; (2): total initial cluster mass derived from evolutionary models; (3): cluster mass derived from stellar velocity dispersion; (4): cluster age; (5): cluster diameter; (6): cluster distance; (7): distance from cluster to the Galactic centre; (8): initial mass range of the RSGs within the clusters. RSGC2 values come from DFK07.

(1) Cluster	(2) M_{init} (evol) ($\times 10^4 M_{\odot}$)	(3) M_{dyn}	(4) Age (Myr)	(5) d (pc)	(6) D_{\odot} (kpc)	(7) D_{GC}	(8) $M_{\text{init}}(\text{RSGs})$ (M_{\odot})
RSGC1	3 ± 1	5 ± 1	12 ± 2	1.5 ± 0.3	6.60 ± 0.89	3.2	18_{-2}^{+4}
RSGC2	4 ± 1	6 ± 4	17 ± 3	$3.2_{-0.7}^{+1.2}$	$5.83_{-0.76}^{+1.91}$	3.5	14 ± 2

4.3. Comparison of the two RSG clusters

Given that, until recently, the largest number of RSGs in any one cluster was 5, the discovery of the two Scutum RSG clusters lying so close to one another is remarkable. After applying the same analysis techniques to each cluster, we summarize the physical parameters of RSGC1 and RSGC2 in Table 3.

The radial velocities of each cluster put them at the tangential point of the Galactic rotation curve, with Galacto-centric distances of 3-4kpc. The clusters are separated from one another by $0.8_{-0.7}^{+1.6}$ kpc. Their proximity, combined with their similar ages, suggests that they were both formed in a region-wide starburst phase some 10-20Myr ago, and that the chemical abundances of their natal material should be similar.

First-order evidence of uniform metallicity between the clusters comes from the median spectral-types of the RSGs, which is M3 in each cluster. The average spectral-type of RSGs has been shown to be dependent on environment, shifting gradually to later types with increasing metallicity – averages of K5, M1, and M2 were found for the SMC, LMC and Galaxy respectively (Elias et al. 1985; Massey & Olsen 2003). Proposed physical explanations for this include (a) reduced metallicity leading to lower envelope opacities, increased stellar radii and hence to systematically lower effective temperatures; or (b) the effect of lower metal abundances on the strengths of the diagnostic TiO lines. Regardless, the average spectral-type of M3 for the two Scutum clusters would seem to suggest that they have similar, possibly super-solar metallicities. The chemical abundances of the stars in these clusters will be the subject of a future paper.

Both from the analysis of evolutionary models, and the velocity dispersion, we find similar masses for each cluster – the factor of two difference in the number of RSGs is caused

by the difference in cluster ages. This may also explain the slightly larger size of RSGC2: it has been suggested by Bastian & Goodwin (2006) that a cluster of this initial mass and age may be *out* of virial equilibrium. This arises when the left-over natal material is expelled from the cluster by the first SNe explosions of the cluster’s most massive stars. This leaves the remaining stars with a velocity dispersion larger than that of a virialized cluster, resulting in cluster expansion. This may explain (i) the slightly different sizes of the clusters, (ii) the apparent lack of any obvious diffuse nebular emission in the GLIMPSE images. Also, we note that the dynamical masses of each cluster are slightly higher than the ‘evolutionary’ masses, though the errors on the dynamical masses, in particular the density parameter η , make it difficult to draw any firm conclusions from this.

The difference in ages between the two clusters implies that the initial masses of the RSGs in each must be different; in the younger RSGC1 we are seeing stars with larger initial masses than in the slightly older RSGC2. To investigate the initial masses of the stars in each cluster, we again use the evolutionary models of Meynet & Maeder (2000). For a given isochrone, we find the minimum and maximum initial masses and luminosities of all stars with effective temperatures cooler than 4000K, i.e. the temperature range of the RSGs. In Fig. 10 we plot the luminosity and mass ranges of cool stars as a function of time. From the luminosity ranges of the stars in each cluster, we then determine the initial masses of the RSGs. For RSGC1 we find $M_{\star,\text{init}} = 18_{-2}^{+4}M_{\odot}$, and for RSGC2 $M_{\star,\text{init}} = 14 \pm 2M_{\odot}$. This underlines the potential importance of the RSG clusters to the study of stellar evolution: *they allow us to study large numbers of RSGs at uniform metallicity as a function of initial mass.*

4.4. Masers in RSGs

One aspect of RSG evolution which the two Scutum RSG clusters allow us to study is the onset of the maser-active phase. Masers are often observed in ‘extreme’ cool stars, e.g. the RSGs VY CMa, NML Cyg, S Per (see Richards & Yates 1998, and refs therein), which are also synonymous with large IR excesses. In the standard picture, these phenomena are caused by episodes of high mass-loss, producing large amounts of circumstellar material which gives rise to the IR excess. The masers themselves originate in the outflowing material. The SiO 43GHz maser is formed low in the wind at higher temperatures; at larger radii the formation of dust grains leads to a depletion of SiO. In the SiO maser-forming region the outflow velocity is low, and hence SiO masers typically have radial velocities similar to the stellar systemic velocity, v_{sys} (Jewell et al. 1991). Higher in the wind the H₂O 22GHz maser forms, and typically has peaks at many velocities between $v_{\text{sys}} \pm v_{\infty}$, where v_{∞} is the

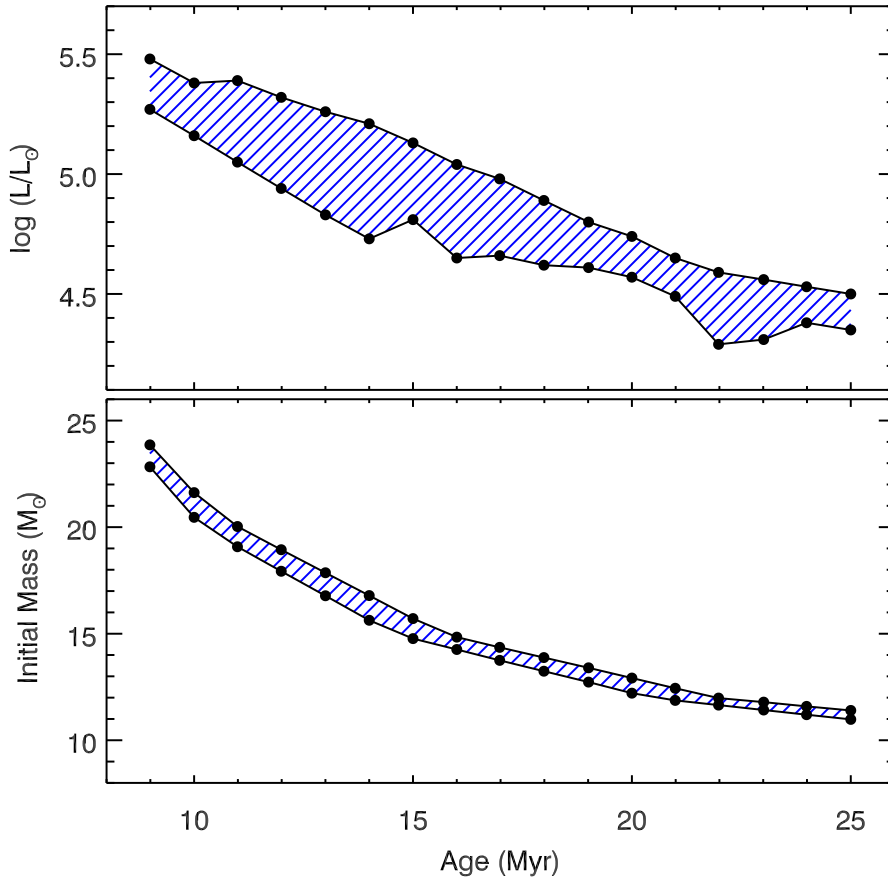


Fig. 10.—: The minimum and maximum luminosities (top panel) and initial masses (bottom panel) of stars with effective temperatures cooler than 4000K in a coeval cluster. Calculated using the rotating Geneva isochrones of Meynet & Maeder (2000).

wind’s terminal velocity (typically around $10\text{-}30\text{ km s}^{-1}$). At larger radii still, H_2O is photo-disassociated to OH, giving rise to the 1612MHz OH maser. Here the outflow has reached its terminal velocity, giving the line-profile its typical double-peaked morphology (where the separation of the peaks is $2v_\infty$ and the centroid is v_{sys}). For a more comprehensive review of masers in luminous cool stars, see Habing (1996).

It is unclear as to whether the maser stage is one which all RSGs will go through, or whether only extreme objects will pass through this phase. Much work has been done on the detailed physical conditions under which masers form (see review of Habing 1996), however in a simplified picture one may say that the presence of the different masers is determined by the wind density, i.e. by mass-loss rate and by pulsations. For an increasing mass-loss rate, gradually the critical density will be reached in the formation zones of each transition;

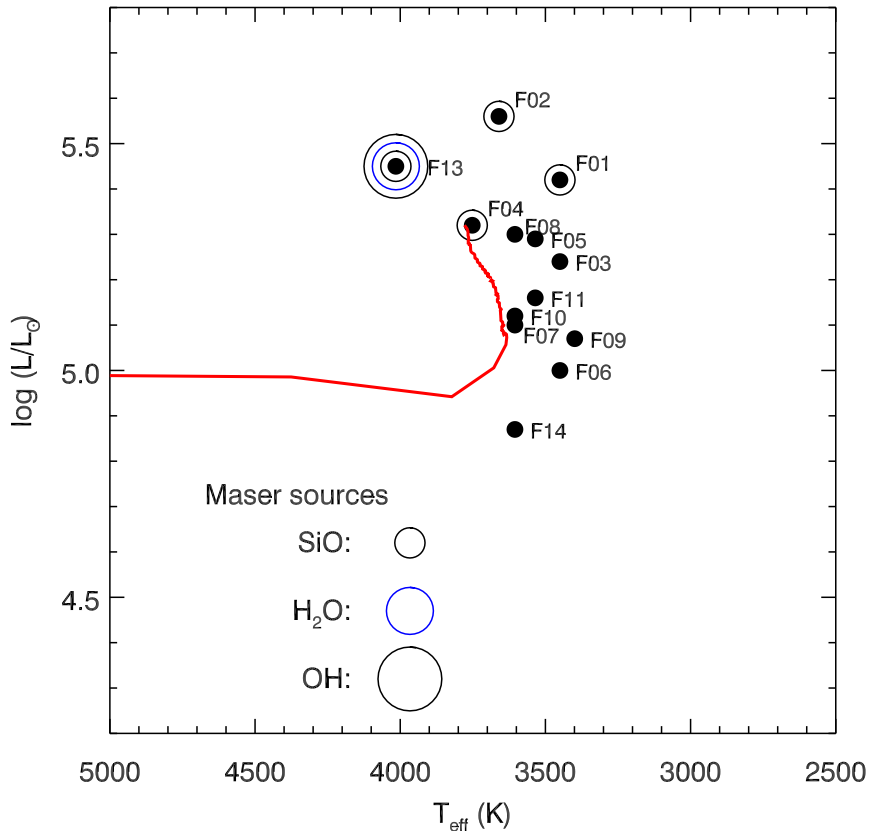


Fig. 11.—: H-R diagram of the RSGs in RSGC1, showing those stars which are maser sources. A 12Myr model isochone is overplotted, from the rotating Geneva models of Meynet & Maeder (2000).

while stellar pulsations will create density-contrasts in the outflow, conducive to population inversions. That is to say that we expect to see maser emission from those RSGs which have the strongest mass-loss rates and which are pulsationally unstable.

Mass-loss from RSGs is driven by radiation pressure on dust grains in the outer atmosphere, and hence depends upon the star’s effective temperature (cool enough to allow dust to form) and luminosity (high radiation pressure) (van Loon et al. 2005). Hence we may expect to find masers in high-mass RSGs which have the higher luminosities, while among a coeval sample of RSGs one may expect to see masers in those objects furthest along their evolution, where their path on the HR diagram takes a sharp upturn (see Fig. 7). Further, as masers are linked to stellar pulsations, we may expect to find masers in unstable stars – i.e. stars with high L_{\star}/M_{\star} ratios that are evolving closer to the Humphreys-Davidson limit at $L_{\star} \sim 10^{5.7} L_{\odot}$ (Humphreys & Davidson 1979). This zone of the H-R diagram is often linked to the so-called

‘modified’ Eddington limit, when the contributions of atomic/molecular transitions to the continuum opacity are included when calculating the Eddington luminosity.

To investigate the presence of masers in RSGs, in Fig. 11 we plot a HR diagram of the RSGs in RSGC1, and indicate those stars which are maser sources. In addition to the OH maser observations presented here, SiO and H₂O maser observations of RSGC1 were also taken by Nakashima & Deguchi (2006). They found that stars F01, F02, F04 and F13 were spatially coincident with SiO emission, while they concluded that the H₂O maser emission they found was likely to come from F13⁴.

The figure shows that it is the most luminous stars of the cluster which exhibit maser emission. Further, F13, which is the source of SiO, H₂O and OH masers, appears to be at the point of evolving back toward the blue. The figure therefore appears to support the hypothesis that maser emission activates (or becomes strong enough to be observed) in the latest stages of RSG evolution, when the star’s mass-loss rate is highest and the star becomes unstable to pulsations.

This hypothesis could be tested with a study of the second Scutum RSG cluster, RSGC2. This cluster also has many RSGs and so we are again seeing stars in both the earlier and later RSG stages. As mentioned in Sect. 4.3, the stars in RSGC2 are less luminous and hence further from the H-D limit. Though they likely have lower initial masses, they have lower L_*/M_* ratios. Thus, we may not expect to see maser emission from these stars, especially those with lower L_* . A comprehensive maser study of the RSGC2 region would be able to test at which phase of RSG evolution stars become maser-active, while non-detections would place lower-limits to the initial-mass requirements to pass through the maser-active phase.

Finally, we note that the YHG F15 is not observed to have maser emission, unlike the prototype post-RSG IRC +10420. Masers are rarely observed around stars hotter than ~ 4000 , and the presence of maser emission in IRC +10420’s outflow is commonly accepted as evidence of its rapid evolution away from the RSG phase. That no maser is observed in F15 may be indicative of a lower wind-density while in the RSG phase, due to its lower initial mass ($\sim 18M_\odot$ compared to $\sim 40M_\odot$ for IRC +10420).

⁴The large beamsize of the 22GHz H₂O maser, 73'', overlaps several other stars in the cluster. However, as these masers are often observed in stars with maser emission from SiO, and as the central velocity of the H₂O maser was consistent with that from the SiO maser emission of F13, Nakashima & Deguchi (2006) concluded that F13 was likely to be the origin of the H₂O maser emission.

5. Conclusions

We have presented a comprehensive investigation into the physical properties of the luminous cool stars in the massive cluster RSGC1. Using high-resolution spectroscopy we have accurately measured the cluster’s radial velocity, derived its kinematic distance, and reappraised the stars’ temperatures and luminosities. We find a larger luminosity spread than in the discovery paper, which is well fitted by a cluster age of 12Myr and cluster mass of $(3 \pm 1) \times 10^4 M_{\odot}$. The mass is similar to that of the nearby cluster RSGC2, and we suggest that the difference in the number of RSGs in each is due to the separation in cluster ages, with RSGC2 being somewhat older. This implies that the initial masses of the RSGs in each cluster are different, which we determine to be $\sim 18 M_{\odot}$ for RSGC1 and $\sim 14 M_{\odot}$ for RSGC2. The clusters therefore allow the study of RSG evolution as a function of initial mass, while constraining the variable of metallicity. Finally, with new 1612MHz radio observations we find compelling evidence that the OH maser is associated with star F13, and collating recent maser observations of the cluster we argue that the maser-active phase is associated with stars in the latter stages of RSG evolution.

Acknowledgments: We would like to thank Maria Messineo for useful discussions concerning masers in cool stars, and the anonymous referee for comments and suggestions which improved the paper. We thank Mark Claussen for discussions regarding the astrometric accuracy of the VLA observations. The material in this work is supported by NASA under award NNG 05-GC37G, through the Long-Term Space Astrophysics program. This research was performed in the Rochester Imaging Detector Laboratory with support from a NYS-TAR Faculty Development Program grant. The National Radio Astronomy Observatory is a facility of the National Science Foundation operated under cooperative agreement by Associated Universities, Inc. Part of the data presented here were obtained at the W. M. Keck Observatory, which is operated as a scientific partnership among the California Institute of Technology, the University of California, and the National Aeronautics and Space Administration. The Observatory was made possible by the generous financial support of the W. M. Keck Foundation. This publication makes use of data products from the Two Micron All Sky Survey, which is a joint project of the University of Massachusetts and the Infrared Processing and Analysis Center/California Institute of Technology, funded by the National Aeronautics and Space Administration and the NSF. This research has made use of MSX and Spitzer’s GLIMPSE survey data, the SIMBAD database, Aladin & IDL software packages, and the GSFC IDL library.

REFERENCES

- Bastian, N. & Goodwin, S. P. 2006, *MNRAS*, 369, L9
- Becker, R. H., White, R. L., Helfand, D. J., & Zoonematkermani, S. 1994, *ApJS*, 91, 347
- Benjamin, R. A., Churchwell, E., Babler, B. L., et al. 2003, *PASP*, 115, 953
- Blommaert, J. A. D. L., van Langevelde, H. J., & Michiels, W. F. P. 1994, *A&A*, 287, 479
- Brand, J. & Blitz, L. 1993, *A&A*, 275, 67
- Davies, B., Figer, D. F., Kudritzki, R.-P., et al. 2007, *ArXiv e-prints*, 708
- Diamond, P. J., Johnston, K. J., Chapman, J. M., et al. 1987, *A&A*, 174, 95
- Egan, M. P., Price, S. D., & Gugliotti, G. M. 2001, in *Bulletin of the American Astronomical Society*, 561–+
- Eisenhauer, F., Genzel, R., Alexander, T., et al. 2005, *ApJ*, 628, 246
- Elias, J. H., Frogel, J. A., & Humphreys, R. M. 1985, *ApJS*, 57, 91
- Feast, M. & Whitelock, P. 1997, *MNRAS*, 291, 683
- Figer, D. F., Gilmore, D., Kim, S. S., et al. 2003, *ApJ*, 599, 1139
- Figer, D. F., MacKenty, J. W., Robberto, M., et al. 2006, *ApJ*, 643, 1166
- Gahm, G. F. & Hultqvist, L. 1976, *A&A*, 50, 153
- Gorlova, N., Lobel, A., Burgasser, A. J., et al. 2006, *ApJ*, 651, 1130
- Habing, H. J. 1996, *A&A Rev.*, 7, 97
- Heger, A., Fryer, C. L., Woosley, S. E., Langer, N., & Hartmann, D. H. 2003, *ApJ*, 591, 288
- Hirschi, R., Meynet, G., & Maeder, A. 2004, *A&A*, 425, 649
- Humphreys, R. M. & Davidson, K. 1979, *ApJ*, 232, 409
- Indebetouw, R., Mathis, J. S., Babler, B. L., et al. 2005, *ApJ*, 619, 931
- Jewell, P. R., Snyder, L. E., Walmsley, C. M., Wilson, T. L., & Gensheimer, P. D. 1991, *A&A*, 242, 211
- Kleinmann, S. G. & Hall, D. N. B. 1986, *ApJS*, 62, 501

- Koornneef, J. 1983, *A&A*, 128, 84
- Kothes, R. & Dougherty, S. M. 2007, ArXiv e-prints, 0704.3073
- Levesque, E. M., Massey, P., Olsen, K. A. G., et al. 2005, *ApJ*, 628, 973
- Levesque, E. M., Massey, P., Olsen, K. A. G., et al. 2006, *ApJ*, 645, 1102
- Massey, P. & Olsen, K. A. G. 2003, *AJ*, 126, 2867
- Mengel, S., Lehnert, M. D., Thatte, N., & Genzel, R. 2002, *A&A*, 383, 137
- Messineo, M., Habing, H. J., Menten, K. M., et al. 2005, *A&A*, 435, 575
- Meynet, G. & Maeder, A. 2000, *A&A*, 361, 101
- Meynet, G., Maeder, A., Schaller, G., Schaerer, D., & Charbonnel, C. 1994, *A&AS*, 103, 97
- Nakashima, J.-i. & Deguchi, S. 2006, *ApJ*, 647, L139
- Oudmaijer, R. D., Davies, B., de Wit, W., & Patel, M. 2008, in *Biggest, Baddest, Coolest stars*, ed. D. Luttermoser, B. Smith, & R. Stencel (ASP Conference series, in press)
- Reid, M. J. & Brunthaler, A. 2004, *ApJ*, 616, 872
- Repolust, T., Puls, J., & Herrero, A. 2004, *A&A*, 415, 349
- Richards, A. M. S. & Yates, J. A. 1998, *Irish Astronomical Journal*, 25, 7
- Rieke, G. H. & Lebofsky, M. J. 1985, *ApJ*, 288, 618
- Salpeter, E. E. 1955, *ApJ*, 121, 161
- Schaerer, D., Charbonnel, C., Meynet, G., Maeder, A., & Schaller, G. 1993, *A&AS*, 102, 339
- Schaller, G., Schaerer, D., Meynet, G., & Maeder, A. 1992, *A&AS*, 96, 269
- Trejo, A. & Rodríguez, L. F. 2006, *Revista Mexicana de Astronomía y Astrofísica*, 42, 147
- van Loon, J. T., Cioni, M.-R. L., Zijlstra, A. A., & Loup, C. 2005, *A&A*, 438, 273
- Wallace, L. & Hinkle, K. 1996a, *ApJS*, 103, 235
- Wallace, L. & Hinkle, K. 1996b, *ApJS*, 107, 312
- Wallace, L. & Hinkle, K. 1997, *ApJS*, 111, 445